EES Catalysis

PAPER

View Article Online
View Journal | View Issue

Cite this: *EES Catal.*, 2026, 4, 146

Unraveling membrane electrode assembly design for electrochemical conversion of carbon dioxide to formate/formic acid

Puvikkarasan Jayapragasam,[a] Jacob A. Wrubel,*[a] Paige Nicole Brimley,[b] Fry Intia,[a] Leiming Hu[a] and Kenneth C. Neyerlin[a]

Received 10th September 2025,
Accepted 23rd September 2025

DOI: 10.1039/d5ey00272a

rsc.li/eescatalysis

This work presents a one-dimensional continuum modeling approach to investigate various cell architectures used for electrochemical conversion of CO_2 to formate/formic acid. Ion transport is simulated by a system of generalized modified Poisson–Nernst–Planck (GMPNP) equations that reflect the reactive transport phenomena including steric effects as the electrolyte solutions become concentrated. In the cathode catalyst layer, ionic current contributions from both the supporting electrolyte and solid-state ionomer are considered. Voltage and CO_2 utilization breakdowns are utilized to deconvolute the impacts of the cell architecture. The origins of (bi)carbonate formation in the cathode are explored, as the subsequent decrease in CO_2 availability is a key reason for low faradaic efficiencies to formate/formic acid. In addition, the role of a supporting electrolyte (KOH) is investigated to understand its tradeoffs: while the K^+ ions can improve both conductivity and electrochemically active surface area in the cathode, the presence of OH^- ions raises the pH and leads to deleterious formation of (bi)carbonates. To this end, we also present parametric studies on the concentration and flow rate of supplied KOH to the cell, to establish a path towards eliminating the need for a supporting electrolyte.

Broader context

Electrochemical CO_2 conversion is a promising electrified pathway for upgrading CO_2 to useful carbon-based chemicals and fuels. Specifically, formic acid is a C1 intermediate that is valuable as a precursor feedstock in biological conversion systems. However, the electrochemical CO_2 reduction reaction produces the formate ion, not formic acid. While the acidification of formate salts can be performed downstream of the reactor, it is more efficient to directly produce and recover formic acid in the same device. In this work, we develop an improved modeling framework and use it to analyze zero-gap CO_2 electrolyzer architectures for their ability to produce recoverable formic acid.

1. Introduction

Electrochemical conversion of CO_2 can be used to create value-added chemicals/fuels such as carbon monoxide,[1–3] methane,[1,2] ethylene,[2] formate/formic acid,[4–8] and other multi-carbon products.[9–11] This electron to molecule conversion technology represents a stable vector for achieving carbon-based fuels and commodities. CO_2 conversion to formate/formic acid has extensive industrial applications including chemical production, cleaning, textiles, and more, which require more than 800 000 metric tons yearly.[12–14] Additionally, formic acid could be suitable for automobile[2,15] and fuel cell[16–18] applications due to its hydrogen content (4.53 wt%).[19] Other advantages of formic acid include its non-toxic nature, biodegradability, and simplified storage and distribution.[20] Perhaps most importantly, formic acid (specifically the acid, not the ion/salt form) is a viable precursor to fatty acids in biological conversion systems.[21–24] In turn, these fatty acids can be upgraded to sustainable aviation fuel or be used in diesel blendstocks. Electrochemical conversion of CO_2 into formate/formic acid is economical,[25,26] reducing production cost by as much as 75% compared to traditional approaches.[23] Electrochemical conversion of CO_2 to formate is a two-electron transfer reaction enabling simplified electrochemical cell design and higher CO_2 conversion rates compared to C_{2+} products that require more complex C–C coupling and multi-electron transfer processes.[27–29] This work explores

[a] *Chemistry and Nanoscience Center, National Renewable Energy Laboratory, Golden, CO, USA. E-mail: jacob.wrubel@nrel.gov*
[b] *Department of Chemical and Biological Engineering, University of Colorado Boulder, Boulder, CO, USA*

the effect of electrochemical cell architectures on CO_2 conversion to formate with the aim of maximizing faradaic efficiency (FE), single pass CO_2 conversion, and formic acid capture.

Numerous studies have been performed to better understand various CO_2 electrolyzer cell architectures, generally aiming to enhance CO_2 conversion and cell performance. Of the available electrochemical cell architectures, membrane electrode assembly (MEA) cells are popular due to their electrical performance and scalability, especially compared to (liquid) H-cell configurations.[30–32] Various components of MEA cells have been investigated to observe their effect on cell performance. For instance, cathode catalyst materials have been engineered to have high selectivity towards carbon products (CO and formate/formic acid) while suppressing the hydrogen evolution reaction (HER).[33,34] Similarly, the role of a supporting electrolyte in the MEA system has been found to improve CO_2 selectivity by improving ionic conductivity in the cathode domain.[35–38] Researchers have identified that KOH can act as an ionophore to facilitate the ion transport and electrochemical conversion processes in the cell.[7] This is an important benefit, as CO_2 solubility and availability in the cathode are critical factors for effective CO_2 conversion. Gaseous CO_2 has two competitive pathways towards consumption, conversion at the catalyst/ionomer interface (two phase boundaries, or "2PB") and the formation of (bi)carbonate ions (dictated by the pH value in the electrolyte).[39] These (bi)carbonate ions then traverse the cell to the anode side, where they exit or release CO_2 gas without undergoing CO_2 conversion to any useful products. Supporting electrolytes also expand the electrochemically active 2PB sites to include catalyst/liquid electrolyte interfaces, instead of just catalyst/polymer electrolytes.[40] In order to minimize (bi)carbonate formation and encourage electrochemical CO_2 conversion, several studies have explored methods to refine the cathode microenvironment by tuning both the catalyst and catalyst layer morphology to enhance CO_2 mass transport and increase the active sites of CO_2/catalyst.[41,42] In the current study, we model several approaches for supplying MEA cell architectures with KOH to observe its effect on CO_2 utilization and the reaction selectivity towards formic acid.

MEA cells also enable the strategic tuning of pH gradients across the system by varying the type of membranes and ionomers used. For example, alkaline conditions in the cathode facilitate the conversion of CO_2 to C_{2+} products by suppressing the HER.[35,36,41,43,44] In addition, alkaline environments feature higher CO_2 solubility. However, acidic conditions are useful for suppressing carbonate formation and providing protons to yield formic acid from formate.[9,36,45] Various attempts have been made to tune the cell design to maximize the benefits from both ends of the pH scale.[30,42,46–48] However, due to the multifunctional nature of CO_2 electrolyzer cells, a clear path forward has not yet been established. For example, an ideal MEA cell for electrochemical conversion of CO_2 to formate/formic acid should:

- exhibit high faradaic efficiency to formate
- exhibit high single-pass CO_2 utilization
- minimize cell voltage
- minimize (bi)carbonate crossover
- facilitate production and removal of highly concentrated formic acid while limiting product oxidation
- exhibit good durability

These criteria can all be influenced by component design choices and operating conditions and present a wide-ranging design space.

While experimental approaches can provide vital information about efficient cell operation,[4,5,42,49] sweeping through extensive test matrices is very resource intensive. In addition, it can be difficult or impossible to directly observe small scale phenomena like concentration and pH gradients, local ion exchange, and reaction fronts. The complex interplay and nonlinearity of physical phenomena in a CO_2 electrolyzer cell (especially in the cathode) can be a hurdle to optimizing the electrolyzer design. Therefore, multiphysics numerical modeling, when closely coupled with experiments, is an extremely valuable tool to accelerate cell architecture design and system optimization. In addition, validated numerical models can be used to perform sensitivity analyses of geometric and morphological parameters, as well as operation conditions.

Poisson–Nernst–Planck (PNP) equations derived from the dilute solution theory are commonly used for numerical modeling of electrolyzer cells.[30,46,50–54] Although the PNP equations capture reactive, multi-species ion migration and the ionic potential distribution in the cell, they fail to capture steric effects from ion–ion interactions as the electrolyte solutions increase in strength.[55,56] The voltage bias during cell operation provides a large driving force to uptake additional ions from available electrolyte reservoirs (*e.g.*, a feed of KOH supporting electrolyte). Under these conditions, a typical PNP approach will incorrectly predict ionic strengths several times higher than the ion exchange coefficient (IEC) of the membrane system being simulated. To overcome this drawback, several other modeling approaches have been recommended. For instance, the generalized modified Poisson–Nernst–Planck (GMPNP) equations have been used to encompass the steric effects and ion accumulation in MEA systems.[57–60] In addition, Frumkin corrected Tafel equations along with the size modified PNP equations (SMPNP) were employed for computing accurate concentration gradients and potential jumps at the outer Helmholtz plane.[61,62] Marcus–Hush–Chidsey (MHC) theory has also been used in CO_2 conversion models to account for solvent molecule reorganization during electron transfer steps.[63]

This work employs a system of GMPNP equations to accurately model various MEA cell architectures during operation. Our unique approach also resolves the multiple ionic pathways in the electrodes: when using a supporting electrolyte, ions in the electrodes can travel through both the ionomer phase and electrolyte filled pores.[40] Many prior works ignore these parallel pathways and the additional mechanisms for ion exchange, which affect the availability of aqueous CO_2 at the electrochemically active 2PBs (catalyst/ionomer and catalyst/electrolyte). Additional currents and reactions are accounted for in each ion conducting domain, leading to a more accurate consideration

of dissolved CO_2 transport and utilization. This increases the model complexity at the membrane and electrode interfaces, so a tractable setup and solution approach is discussed in this work.

2. Methods

2.1. Cell architectures

Fig. 1 shows sketches of three different MEA cell architectures that were chosen to be investigated in this work based on the availability of experimental data. Fig. 1a depicts an anion exchange membrane (AEM) architecture supported by a stainless steel (SS) mesh on the anode side. The anode is supplied with a potassium hydroxide (KOH, 50 ml min^{-1}) supporting electrolyte, which allows the SS mesh to catalyze the oxygen evolution reaction (OER). Humidified CO_2 is supplied to the cathode side. The cathode catalyst layer (CCL) is a typical multiphase porous composite, featuring Bi_2O_3 as the catalyst material and an AEM ionomer as the binder. This configuration is referred to as the AEM-OER cell in this work.

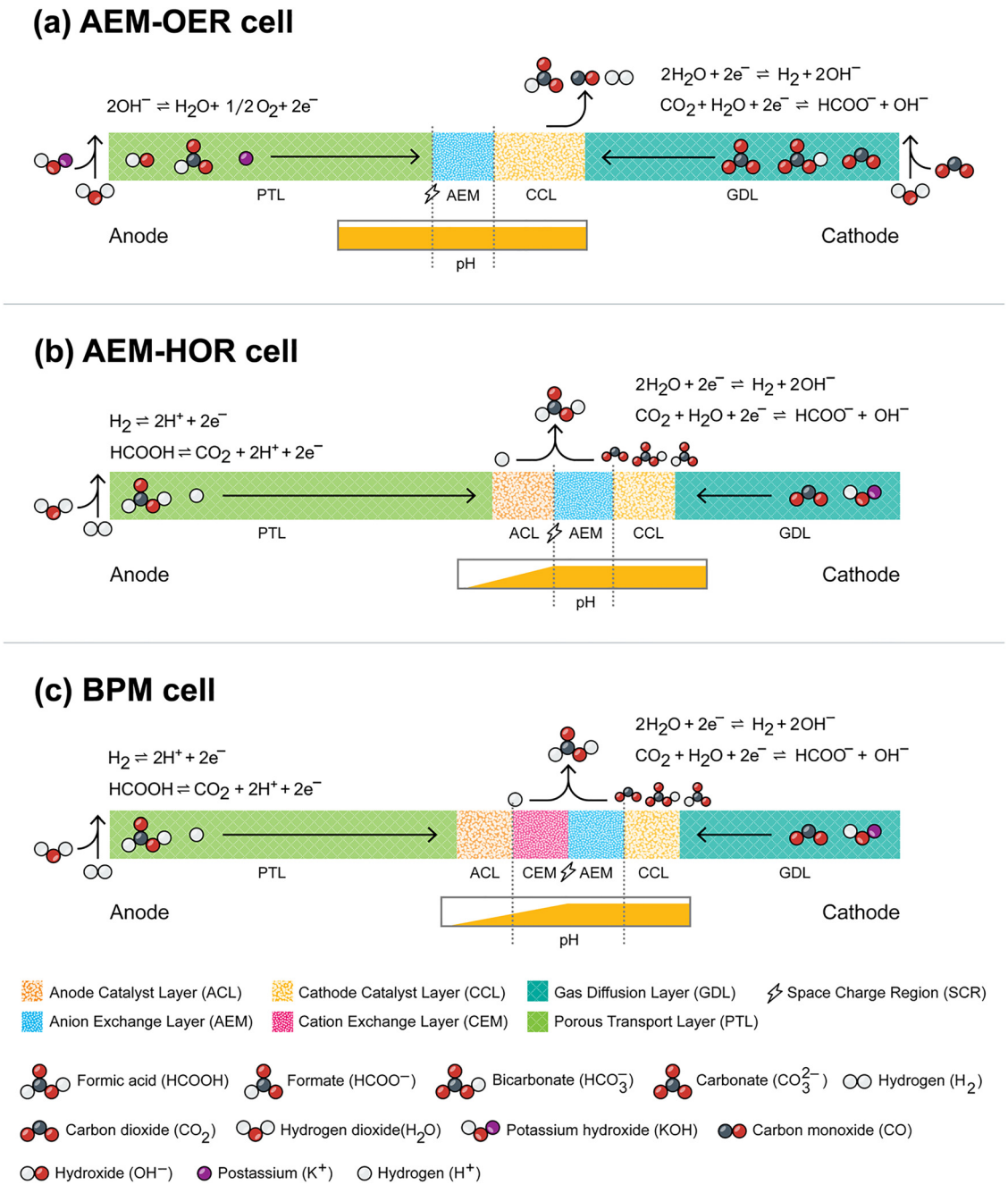

Fig. 1 Schematic representations of (a) AEM-OER, (b) AEM-HOR and (c) forward bias BPM cell architectures studied in this work shown with electrolyte feed directions and pH variation.

Fig. 1b depicts a different AEM architecture with composite (pore/ionomer/catalyst) catalyst layers for both the electrodes. This architecture is supplied with humidified H_2 on the anode side to perform hydrogen oxidation (HOR) and is referred to as the AEM-HOR cell. The cathode side of the AEM-HOR cell is supplied with humidified CO_2 and a small amount (2 ml min^{-1}) of aqueous KOH.

Fig. 1c depicts a bipolar membrane (BPM) cell architecture under forward bias that features anion exchange and cation exchange membrane layers (AEL, CEL respectively) sandwiched between composite catalyst layers for each electrode. This architecture is referred to as the BPM cell. Like the AEM-HOR cell, the BPM cell is supplied with humidified hydrogen at the anode to perform the HOR. Humidified CO_2 and a small amount (2 ml min^{-1}) of aqueous KOH are supplied to the cathode. The motivation for including this BPM cell architecture is to emphasize the need for a perforated CEL in the BPM cell[5] by analyzing the cell failure mechanism without perforation. The composition of catalyst layers and other cell architecture details are detailed in a previous study[5] and are also included in the SI under Section S1 and Table S2. In the SI, the modeling capabilities were extended to other cell architectures, such as a CEM-OER cell; a detailed discussion is presented in Section S2. The CEM-OER cell features a cation-ion exchange membrane with a liquid electrolyte (KOH) fed to the anode. This cell is not featured in the main text due to excess salt precipitation at the cathode flow fields (as shown in Fig. S3).

The cells in Fig. 1 feature several instances of liquid junctions, which arise at the intersections of dissimilar ionic conductors. For example, the PTL|AEM boundary in Fig. 1a features a transition from aqueous KOH to the solid AEM electrolyte, and the CEL|AEM boundary in Fig. 1c features a transition from the CEL to AEL environment. At these interfaces, space charge regions (SCRs) arise due to the balance of diffusion and migration driving forces. The SCRs, which are indicated by the (⚡) symbol in Fig. 1, feature sharp gradients in both species concentrations and electrostatic potential due to the deviation from local electroneutrality.

2.2. Governing equations

The species concentrations and electrolyte potential distributions in the cell were solved using generalized modified Poisson–Nernst–Planck (GMPNP). The GMPNP equations do not enforce an assumption of electroneutrality everywhere, which allows for the direct simulation of the SCRs. Electroneutrality is observed in the bulk of the domains as a consequence of the Poisson equation. The modeling approach includes the following assumptions:

(1) the ionomer and liquid electrolyte are treated as continuous phases in the CCL region to simplify the porous media homogenization approach

(2) the cathode and anode are assumed to be completely flooded with a liquid electrolyte

(3) the membrane is considered to be fully hydrated with no variation in the water content

(4) the morphology/topology of the porous media are accounted for using a Bruggeman factor to derive effective diffusivities

(5) dielectric permittivity is considered as constant for the phases considered in this study

(6) informed by experimental observation, salt formation and precipitation is ignored for the cell configurations discussed here.

Conservation of aqueous species is given by eqn (1)[45,63,64]

$$\frac{\partial c_i}{\partial t} + \nabla(J_i) = \dot{R}_i \tag{1}$$

where c_i is the concentration of species 'i' and J_i is the molar flux, modeled using the modified Nernst–Planck equation:[57–60]

$$J_i = -D_i\left(\nabla c_i + \frac{c_i z_i F}{RT}\nabla\phi - c_i\left(\frac{N_A\sum_{j=1}^{n} a_j^3\nabla c_j}{1 - N_A\sum_{j=1}^{n} a_j^3 c_j}\right)\right) \tag{2}$$

where D_i is the diffusion coefficient, F is Faraday's constant, R is the gas constant, T is the temperature, ϕ is the potential in the ion-conducting phase, N_A is Avogadro's number, a_j is the hard sphere radius of the ionic species, and z_i is the valence. Eqn (1) and (2) are solved for 8 aqueous species: $i = CO_{2(aq)}$, H^+, OH^-, HCO_3^-, CO_3^{2-}, $HCOO^-$, HCOOH, and K^+. The source term, $\dot{R}_i$, in eqn (1) is comprised of electrochemical and chemical reactions defined below. In eqn (2), Fickian diffusion is accounted for by the first term on the right side, the second term accounts for ion migration under an electric field, and steric effects in concentrated electrolytes are accounted for by the third term. Without the steric effect term, eqn (2) reduces to the conventional Nernst–Planck (NP) equation. A comparison between the GMPNP and NP results is given in Section S3 in the SI.

The ionic potential is solved using the Poisson equation for electrostatics,

$$-\nabla^2\phi_k = \frac{F}{\varepsilon}\sum_i z_i c_{i,k} \tag{3}$$

where ε is the permittivity and the subscript k refers to the ion conducting phase. This work features several different ion conducting phases, including the ionomer (IM) in the catalyst layers, supporting liquid electrolyte (LE), AEL, and CEL.

The mixture averaged diffusion model was used to govern the transport of gaseous species in the GDL domains,

$$J_i = -\left(\rho_g D_i^{eff}\nabla\omega_i + \rho_g\omega_i D_i^{eff}\frac{\nabla M_n}{M_n}\right) \tag{4}$$

where ρ_g is the total gas density, D_i^{eff} is the effective diffusivity computed using Maxwell–Stefan diffusivities, ω_i is the mass fraction, and M_n is the average molar mass of the mixture. Eqn (4) is solved for 4 gaseous species: $i = CO$, H_2, H_2O and CO_2.

2.2.1. Electrochemical reactions. Eqn (5)–(8) and Table 1 list the electrochemical reactions considered at the cathodes and anodes, respectively, studied in this work. The cathodes are mixed potential electrodes, where we assume three possible

Table 1 Electrochemical reactions at the anode

Anode
$2OH^- \rightleftharpoons H_2O + 1/2O_2 + 2e^-$ (for the AEM-OER cell)
$H_2 \rightleftharpoons 2H^+ + 2e^-$ (for the AEM-HOR and BPM cells)
$H_2 + 2OH^- \rightleftharpoons 2H_2O + 2e^-$ (for the AEM-HOR and BPM cells)
$HCOOH \rightleftharpoons CO_2 + 2H^+ + 2e^-$ (for AEM-HOR and BPM cell)

reactions: CO_2 conversion to CO, CO_2 conversion to formate, and the hydrogen evolution reaction (HER). Both acidic and alkaline pathways are considered for the HER, so that all pH ranges can be simulated. The anodes feature the alkaline OER for the AEM-OER cell and the HOR (both acidic and alkaline pathways) for the AEM-HOR and BPM cells.

$$CO_2 + H_2O + 2e^- \rightleftharpoons CO + 2OH^- \quad (5)$$

$$CO_2 + H_2O + 2e^- \rightleftharpoons HCOO^- + OH^- \quad (6)$$

$$2H_2O + 2e^- \rightleftharpoons H_2 + 2OH^- \quad (7)$$

$$2H^+ + 2e^- \rightleftharpoons H_2 \quad (8)$$

Butler–Volmer equations are used to express the electrochemical reaction rates. For CO_2 conversion, these are

$$i_{HCOO^-} = i^0_{HCOO^-} \times \left(\frac{c_{HCOO^-}}{c_{ref}}\frac{c_{OH^-}}{c_{ref}} \times \exp((1-\alpha_{HCOO})f\eta_{HCOO}) - \frac{c_{CO_2}}{c_{ref}} \times \exp(-\alpha_{HCOO}f\eta_{HCOO})\right) \quad (9)$$

$$i_{CO} = i^0_{CO} \times \left(\left(\frac{c_{OH^-}}{c_{ref}}\right)^2 \times \exp((1-\alpha_{CO})f\eta_{CO}) - \frac{c_{CO_2}}{c_{ref}} \times \exp(-\alpha_{CO}f\eta_{CO})\right) \quad (10)$$

where $f = F/RT$. For the HER and HOR, the Butler–Volmer expressions are:

$$i_{HER,A} = i^0_{HER,A} \times \left(\frac{c_{H_2}}{c_{ref}} \times \exp\left((1-\alpha_{HER,A})f\eta_{HER,A}\right) - \left(\frac{c_{H^+}}{c_{ref}}\right)^2 \times \exp\left(-\alpha_{HER,A}f\eta_{HER,A}\right)\right) \quad (11)$$

$$i_{HER,B} = i^0_{HER,B} \times \left(\left(\frac{c_{OH^-}}{c_{ref}}\right)^2 \times \exp\left((1-\alpha_{HER,B})f\eta_{HER,B}\right) - \exp\left(-\alpha_{HER,B}f\eta_{HER,B}\right)\right) \quad (12)$$

Eqn (9)–(12) model CO_2 conversion to formate, CO_2 conversion to CO, HER/HOR (acidic) and HER/HOR (alkaline), respectively. In the anode of the AEM-OER cell, the OER rate is

$$i_{OER} = i^0_{OER} \times \left(\exp((1-\alpha_{OER})f\eta_{OER}) - \left(\frac{c_{OH^-}}{c_{ref}}\right)^2 \times \exp(-\alpha_{OER}f\eta_{OER})\right) \quad (13)$$

And in the anode of the AEM-HOR and BPM cell, the formic acid to CO_2 rate is

$$i_{CO_2} = i^0_{CO_2} \times \left(\left(\frac{c_{H^+}}{c_{ref}}\right)^2 \exp\left((1-\alpha_{CO_2})f\eta_{CO_2}\right) - \left(\frac{c_{HCOOH}}{c_{ref}}\right) \times \exp\left(-\alpha_{CO_2}f\eta_{CO_2}\right)\right) \quad (14)$$

The reference concentration, c_{ref}, is taken as 1 M. The overpotentials in eqn (9)–(14) are of the form $\eta_k = \phi_{C/A} - \phi_k - E^0_i$, where $\phi_{C/A}$ is the electronic potential in either cathode or anode, ϕ_k is the ionic potential in domain 'k' (where k = LE or IM), and E^0_i is the standard equilibrium potential for the reaction.

2.2.2. Chemical reactions. Several homogenous reactions are considered to account for the aqueous species interactions, as listed below. Eqn (15) is the autoionization of water, eqn (16)–(19) reflect the acid–base equilibria of aqueous CO_2, and eqn (20) is the association/dissociation of formic acid. KOH is assumed to remain fully dissociated everywhere. The local pH is directly given by the H^+ and/or OH^- concentration, which impacts the formation of (bi)carbonates and hence controls the utilization of carbon dioxide.

$$H^+ + OH^- \rightleftharpoons H_2O \quad (15)$$

$$CO_2 + OH^- \rightleftharpoons HCO_3^- \quad (16)$$

$$HCO_3^- + OH^- \rightleftharpoons CO_3^{2-} + H_2O \quad (17)$$

$$HCO_3^- + H^+ \rightleftharpoons CO_2 + H_2O \quad (18)$$

$$CO_3^{2-} + H^+ \rightleftharpoons HCO_3^- \quad (19)$$

$$HCOO^- + H^+ \rightleftharpoons HCOOH \quad (20)$$

The rates of eqn (15), (18), and (20) are affected by the local electric field strength through the second Wien effect (SWE). Therefore, their forward rate constants are modified by the following factor,[54,65]

$$r_{SWE} = \sum_{n=1}^{\infty} \frac{b^{n-1}2^{n-1}}{n!(n-1)!} \quad (21)$$

where $b = (0.09636 \times E)/(\varepsilon_r T^2)$ and ε_r is the relative permittivity of the electrolyte. The SWE impact is shown in Section S4 of the SI. It was noted that the cells with hydrogen feed at the anode have the r_{SWE} factor more than 20 in some locations.

In both electrodes, the rate of phase change of gaseous CO_2 to/from aqueous form is modeled using the following rate expression:

$$\dot{R}_{CO_2} = k_{CO_2}(H_{CO_2}CO_{2,g} - CO_{2,aq}) \quad (22)$$

where k_{CO_2} is a rate constant and the first term in the parenthesis represents the equilibrium aqueous CO_2 concentration as given by Henry's law. The CO_2 availability plays a crucial role in the cell architectures, especially in the AEM-HOR and BPM cells and the results are explored more in Section S5 of the SI.

2.3. Reaction kinetics between the cathode catalyst ionomer and the liquid electrolyte

A key innovation in the present work is the incorporation of ion transfer between the IM and LE in the cathode. The ionic species in the IM may exchange to and from the LE due to gradients in the concentration and ionic potential. A schematic representation of these transfer phenomena is shown in Fig. 2. Since the ionomer coverage (dark blue region) is not uniform over the catalyst (pink spheres), some parts of the catalyst surface are exposed to LE (light blue region) in the pore domain. Therefore, two different two-phase boundaries are assumed to be electrochemically active in this work: (i) catalyst|LE (represented by the lime green symbols) and (ii) catalyst|IM (represented by the golden yellow symbols). The black arrows depict the pathways for ion transfer within the cathode, including diffusion/migration through the LE, diffusion/migration through the IM, and exchange between the LE|IM. The kinetics for ion transfer between the IM and LE is expressed like a reaction source term,[40]

$$R_{ex} = k_{ex} \times (c_i^{IM}\kappa_i - c_i^{LE}) \quad (23)$$

where k_{ex} is the rate constant, c_i^{IM} and c_i^{LE} are concentrations of ions in IM and LE, respectively, and κ_i reflects the potential gradient between the IM and LE and is expressed as

$$\kappa_i = \exp\left(\frac{n_i F}{RT} \times (\phi^{IM} - \phi^{LE})\right) \quad (24)$$

In eqn (22) and (23), both the concentrations and potential gradients act as driving forces for the ion exchange. Similar expressions are included for ion exchange between the membrane and LE. These three 2D interfaces between the LE, IM and membrane reflect a complicated series of ion exchange processes in the cathode electrode, which will be given careful attention in the following section.

2.3.1. Current balance at two-phase interfaces. To govern the ion exchange processes in the cathode, global ionic charge conservation is invoked by stipulating that the ionic current densities at each interface must sum to the total cell current density. This is expressed as

$$i_{tot} = i_{mem} = i_{IM} + i_{LE} \quad (25)$$

where i_{tot} is the total cell current, i_{mem} is the net ionic current entering the membrane, i_{IM} is the net ionic current entering the IM phase, and i_{LE} is the net ionic current entering the LE phase. Fig. 3 shows a schematic of these pathways.

Eqn (25) solves for the unknown proportions of ionic current entering the IM and LE, not only at the membrane|CCL interface, but throughout the entire CCL as well. This analysis must be included to incorporate the homogenized effects of the catalyst layer morphology, such as 2PB surface areas and tortuosity, into the model.

3. Results and discussion

COMSOL Multiphysics®[66] was used for solving the nonlinear governing eqn (1)–(24) using the general form PDE and transport of concentrated species modules. For the parameter fitting and validating the model against the experimental data, the COMSOL model was integrated with Python using the MPh interface.[67] A modified trust-region optimization technique with complex step differentiation (CSD) is employed for the parameter approximation and model validation.[68,69] A detailed explanation on the optimization technique and statistical analyses is given in the SI (Section S17). A mesh independence study was also performed for the AEM-OER cell to choose the optimal number of elements, and it was found that more than

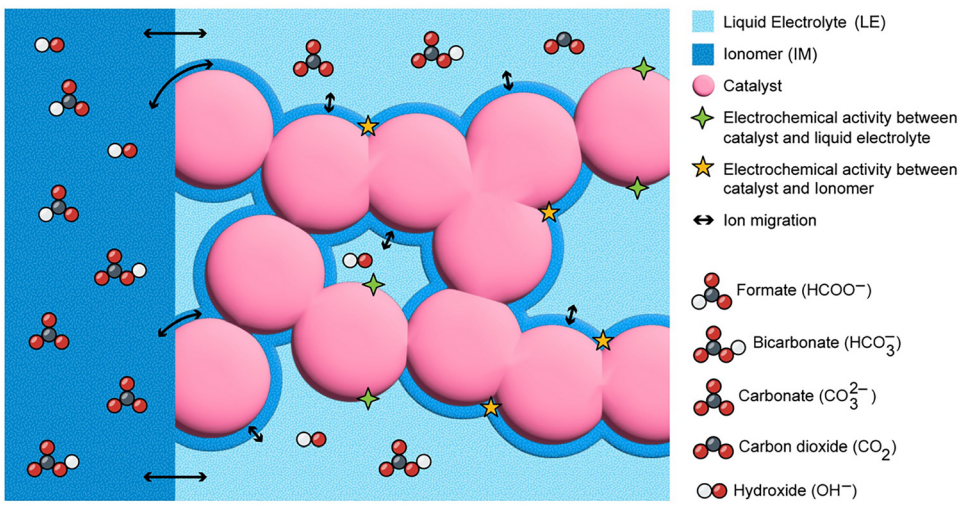

Fig. 2 Ion transfer phenomena in the cathode (catalyst, ionomer, and liquid electrolyte).

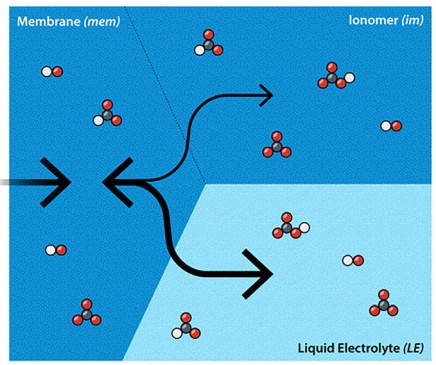

Fig. 3 Flux conditions at the membrane, ionomer and liquid electrolyte interface.

500 elements are sufficient to minimize changes in the voltage and partial current density values (Section S18 in the SI).

3.1. Model validation

Using the Python optimization code, the models for each cell architecture were validated against experimental measurements of polarization curves and partial current densities. Fig. 4 gives an overview of these results: Fig. 4a shows the polarization curves and Fig. 4b–d show the partial currents for the AEM-OER, AEM-HOR, and BPM cells, respectively. In Fig. 4a, the AEM-HOR cell exhibited the lowest cell voltages at low current densities, due to the H_2-fed anode which lowers the equilibrium cell voltage. However, at moderate current densities ($\geq$0.3 A cm^{-2}), the AEM-OER cell featured the lowest overall cell voltage. This is because the AEM-OER cell exhibits a flatter VI curve, which is attributed to the good OER kinetics and CO_2 availability for $HCOO^-$ generation at the cathode. In contrast, the AEM-HOR cell exhibits a steeper VI curve, which is attributed to decreasing CO_2 availability in the cathode as well as the onset of formic acid oxidation in the anode. More detailed voltage breakdown analyses will be presented in a later section. Due to functionality limitation of BPM (which will also be discussed in the ensuing sections), only one data point was available for the BPM cell polarization curve.

Fig. 4b shows partial current densities from the AEM-OER cell, in which we observe good agreement between the model and experiment. Formate production contributes more than 80% of the total current density at 0.5 A cm^{-2}, with the remaining current coming from the HER and CO_2 conversion to CO production. The formate partial current linearly increases with increasing total cell current, with no signs of tapering off. In contrast, Fig. 4c shows the partial currents for the AEM-HOR cell, in which the formate partial current reaches a plateau with increasing cell current as the HER current density increases monotonically. The plateau in the formate generation rate is attributed to higher (bi)carbonate formation in the cathode, which is approximately 3.2 times higher in the AEM-HOR cell

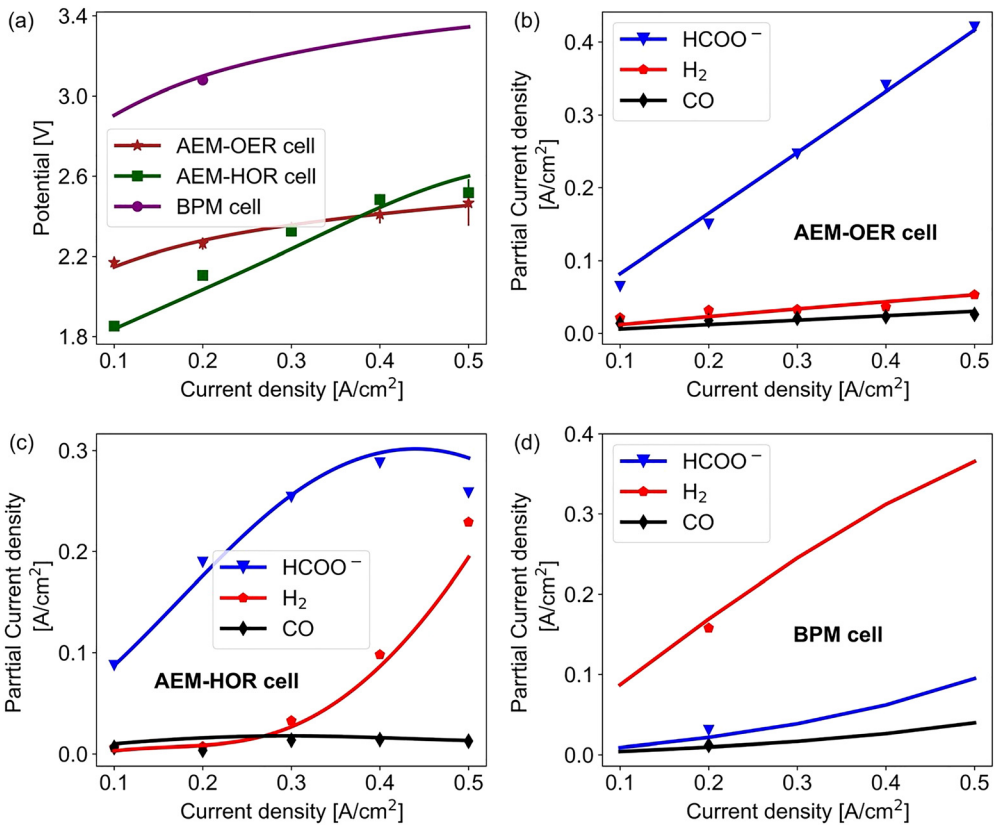

Fig. 4 Simulated *vs.* experimental data for various cell architectures including (a) polarization curves and partial current densities for (b) AEM-OER cell (c), AEM-HOR cell, and (d) forward bias BPM cell. Symbols represent experimental data and solid lines represent simulation results.

than the AEM-OER cell (shown in Fig. S10). Fig. 4d shows the partial currents from the BPM cell, for which only one experimental data point could be obtained before the cell failed.

The results shown in Fig. 4, including both the polarization curve and partial current densities, indicate that the model can replicate experimental data across a wide range of cell architectures. Moreover, the partial current densities in the anodes of the AEM-HOR and BPM cells were also validated to get more accurate kinetic parameters. These validation results are discussed in the SI under Section S6, Fig. S7. The modeling results were extended beyond the experimental operating current density (0.5 A cm^{-2}) for the AEM-OER and AEM-HOR cells. It was found that the AEM-HOR cell completely switches selectivity from CO_2 reduction to the HER. The results are discussed in more detail in the SI under Section S7. The adjusted kinetic parameters for the cathode are given in Table 2 and further parameters are listed in Table S3 in the SI. The adjusted kinetic parameters show a strong dependency on local pH as shown in Fig. S24.

3.2. Concentration profiles

To better understand the transport processes governing the performance of the CO_2 conversion cells, the model can be used to visualize species concentrations in various components. Fig. 5 shows aqueous species concentration profiles at 0.5 A cm^{-2} as a function of cell location. The thickness of every component in the cell architectures is different, and the details are listed in Table S2. The CCL region depicted in these plots corresponds only to the IM phase. Fig. 5a shows that in the AEM-OER cell, the formate ion is the dominant anion throughout most of the MEA, balanced by a high concentration of K^+ ions. There is also a significant amount of CO_3^{2-} in the AEM and CCL. In the PTL (which acts as the anode in this cell configuration), there are two reaction fronts that reflect the (bi)carbonate buffering reactions. Near the PTL|AEM interface ($\sim$125–250 μm), CO_3^{2-} coming from the AEM are converted to HCO_3^- as they encounter the moderately alkaline (almost neutral pH) region of the PTL (see Fig. 7 for the corresponding pH profiles). Closer to the anode boundary ($\sim$0–125 μm), the KOH from the external feed raises the pH, which causes HCO_3^- to be converted back to CO_3^{2-}. Some of this CO_3^{2-} leaks into the anode exhaust stream and represents CO_2 that is lost to (bi)carbonate crossover with an average flux of 0.01 mol $(m^2\ s)^{-1}$ ($\sim$0.1 $mA_{eq}\ cm^{-2}$) over the operating current density range.

A large amount of K^+ ions permeate the entire MEA, including the AEM. The accumulation of K^+ in the AEM occurs as the membrane's selectivity breaks down due to the generation of large amounts of anions. In the CCL, the chemical reaction of CO_2 to CO_3^{2-} and electrochemical $HCOO^-$ production produce enough anions to exceed the ion-exchange capacity (IEC) of the membrane. These anion-producing reactions, as well as the negative ionic potential gradient from the anode to cathode (see Fig. S20), all lead to a large amount of K^+ in the system. The upper concentration limit of about 2.5 M in the system arises due to steric effects at high ionic strengths. These steric effects are captured by the additional term in the generally modified Nernst–Planck equation (eqn (2)). The ion transfer between the IM phase and LE inside in the CCL region is governed by eqn (23) and (24). Concentration profiles in the LE phase for the AEM-OER cell are shown in Fig. S8 in the SI.

The concentration profiles for the AEM-HOR cell are shown in Fig. 5b. Unlike the AEM-OER cell, this architecture featured an anode catalyst layer with an acidic ionomer binder. In this architecture, the CO_3^{2-} anion is dominant in the cathode and membrane domains (250–287 μm) with concentrations reaching close to 0.7 M (similar to Fig. 5a). In addition, the K^+ concentration is much lower compared to the AEM-OER cell due to the lower rates of supporting electrolyte feed at the cathode. In this cell, the anode catalyst layer (235–250 μm) maintains acidic conditions, with H^+ reaching concentrations around 0.8 M. This gives rise to a large pH gradient, ranging from moderately alkaline in the CCL and membrane transiting to strongly acidic in the ACL (as shown in Fig. 7). The sharp drop in pH at the ACL|AEM interface results in a large reaction front where CO_3^{2-} reacts with H^+ to evolve CO_2 gas in the ACL domain. This represents another mechanism for CO_2 crossover that is distinct from (bi)carbonate migration.

The FE to $HCOO^-$ is slightly lower in the AEM-HOR cell, so the cathode and membrane domains show lower $HCOO^-$ concentrations (0.64 M) compared to the AEM-OER cell. In Fig. 5b it can be seen that the incorporation of an acidic anode that produces H^+ from the HOR successfully produces formic acid at the ACL|AEM interface, following eqn (20). The production of formic acid at this interface also leads to a moderate conversion of CO_3^{2-} to HCO_3^- (260–275 μm) as some of the formic acid dissociates, providing H^+, as it back diffuses

Table 2 Estimated kinetic parameters for the cell architectures

		Cell configuration		
Property estimated	Unit	AEM-OER cell	AEM-HOR cell	BPM cell
Exchange current density: formate $\left(I^0_{CO_2For}\right)$	A m^{-2}	0.0289	0.0206	0.0214
Charge transfer coefficient in the ionomer: formate (α_{CO_2For})	—	0.378	0.224	0.148
Exchange current density in the ionomer: carbon monoxide $\left(I^0_{CO_2CO}\right)$	A m^{-2}	0.1347	0.0883	0.0964
Charge transfer coefficient in the ionomer: carbon monoxide (α_{CO_2CO})	—	0.342	0.182	0.140
Exchange current density in the ionomer: basic hydrogen evolution reaction ($I^0_{HER(B)}$)	A m^{-2}	0.0968	0.0714	0.0713
Charge transfer coefficient in the ionomer: basic hydrogen evolution reaction ($\alpha_{HER(B)}$)	—	0.357	0.182	0.124

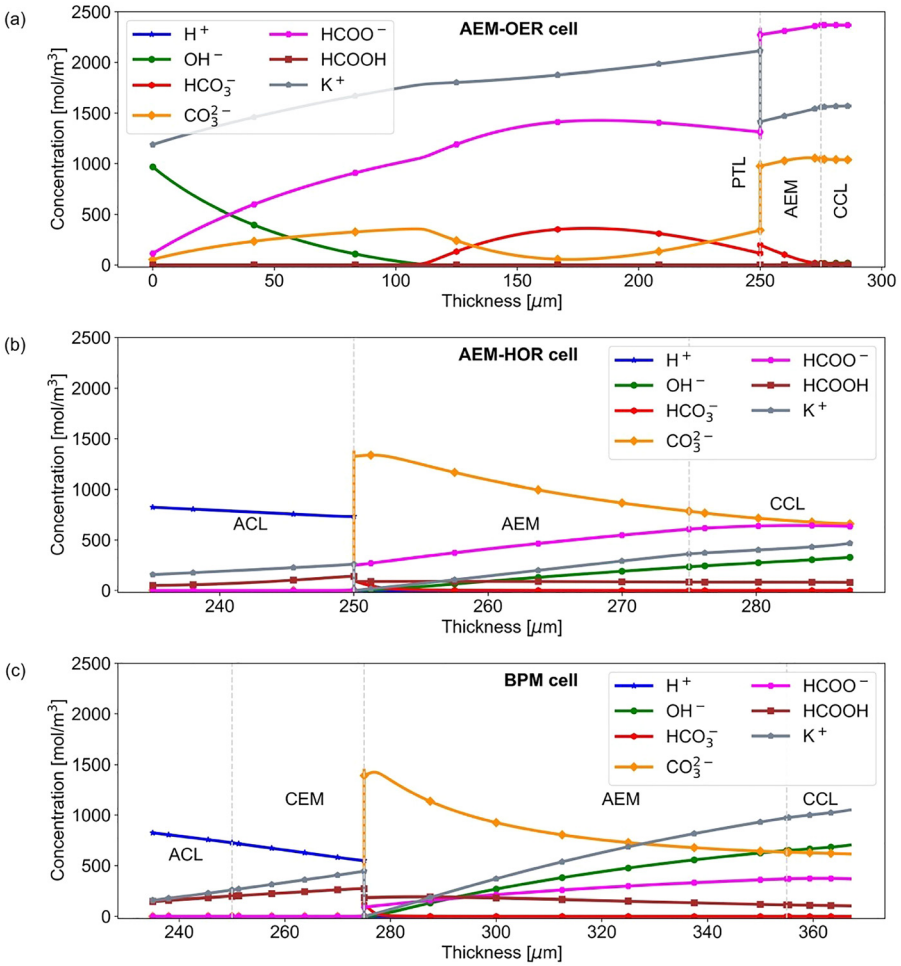

Fig. 5 Concentration profiles for ions in the AEM-OER cell (a), AEM-HOR cell (b) and BPM cell (c) operated at 0.5 A cm^{-2}.

towards the CCL. Moreover, some formic acid (FA) oxidizes at the anode catalyst to generate more CO_2 and H^+ causing further depletion of formic acid in the ACL region (235–250 μm). The amount of FA oxidation ranges from 12 to 77% over the simulated current density range. The cell design could be further refined in the future to minimize this loss of formic acid and instead remove it from the anode as quickly as possible.

Fig. 5c shows ionic concentration profiles for the BPM cell. Although the BPM cell is not stable due to gas bubble accumulation and membrane delamination at higher current densities, the numerical model can still be used to visualize how the cell would have operated. In general, the trends are similar to the AEM-HOR cell with few variations. Unlike the AEM-HOR cell, K^+ is the dominant cation in the system and reaches up to 1 M in the cathode region (~355–367 μm) and steadily decreases toward the CEL|AEL interface (275 μm). CO_3^{2-} and OH^- are the dominant anions in the CCL domain and reach up to ~0.65 M. Like K^+, the OH^- concentration also steadily decreases toward the CEL|AEL interface whereas CO_3^{2-} increases reaching a maximum value of 1.4 M. The main reason for the elevated OH^- concentration in the CCL compared to the AEM-HOR cell is due to the greater alkaline HER reaction rates, as shown in Fig. 4d. As a result, a large amount of K^+ cations from the ACL migrate to the AEL and CCL domains to maintain charge neutrality. At the CEL|AEL interface, CO_3^{2-} ions coming from the CCL meet the H^+ produced in the anode and they rapidly recombine to form CO_2 gas. With no other features or processes to mitigate this phenomenon, this was likely the cause of the BPM cell failure.

To further investigate the distribution of CO_2 in the system, aqueous CO_2 concentration profiles are shown in Fig. 6 for the different cell architectures. For the AEM-OER cell, Fig. 6a, the CO_2 concentration is at a maximum in the CCL domain and tapers to very low values in the anode and AEM due to its consumption in electrochemical CO_2 conversion and HCO_3^-/CO_3^{2-} formation. In contrast, both the AEM-HOR and BPM cells feature spikes in the aqueous CO_2 concentration at the ACL|AEL and CEL|AEL interfaces, respectively. These spikes are the result of CO_3^{2-} and H^+ recombination (these two cell architectures both feature acidic anodes). The reason for the BPM cell failure can be observed from the CO_2 concentration profile at the CEL|AEL interface in Fig. 6c. A significant amount of gaseous CO_2 is generated with nowhere to escape, instead

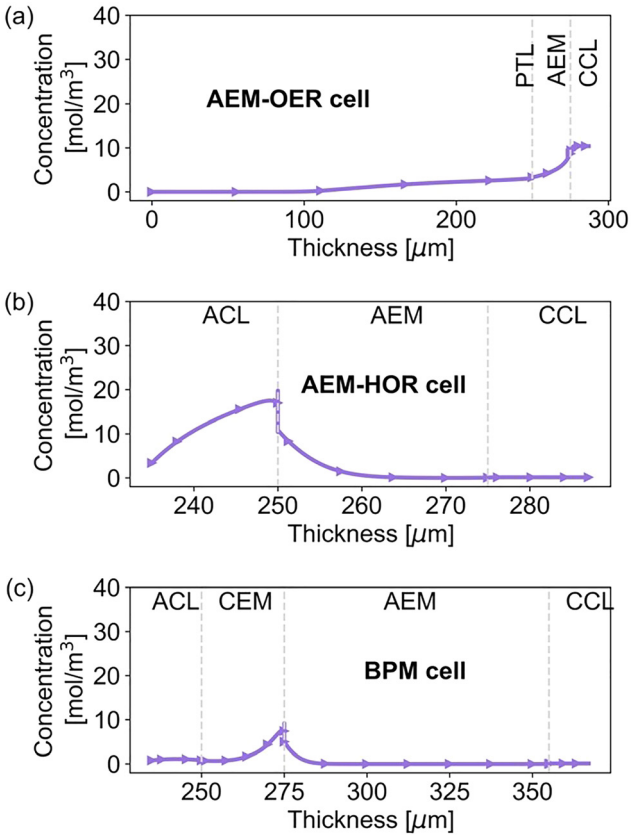

Fig. 6 Aqueous CO_2 concentrations across the (a) AEM-OER cell, (b) AEM-HOR cell, and (c) BPM cell operated at 0.5 A cm^{-2}.

building pressure until the BPM delaminated and ruptured. The phase conversion of aqueous CO_2 to gaseous phase for all cell architectures as a function of current density is discussed in detail in the SI in Section S10. The study demonstrates that increasing gas pressure at the interface is the primary reason for BPM cell failure. The AEM-HOR cell, Fig. 6b, features a similar phenomenon at the ACL|AEM interface, except that in this case the CO_2 generated was free to escape through the porous ACL. This is why perforated membrane layers have been developed for BPM systems to facilitate the release of excess gas and avoid this problem.[5] Although the BPM cell does successfully produce some formic acid at the CEL|AEL interface, it does not exhibit very high FE to formate in the CCL domain due to the following reasons, (i) back diffusion of formic acid (FA) from the CEL|AEL interface and dissociation of FA into $HCOO^-$ and H^+ (eqn (20)) in the CCL domain restricts the forward electrochemical reaction for CO_2 conversion into $HCOO^-$ (eqn (6) and (9)) due to higher $HCOO^-$ concentration, (ii) the dissociated H^+ reacts with OH^- to form H_2O (eqn (15)) to favor the forward basic HER reaction (eqn (7)) and eventually making the cell to switch its affinity from CO_2 conversion reactions to the HER reaction, and (iii) we also speculate that back diffusion of FA can restrict the flow rate of the incoming liquid electrolyte, which reduces the electrochemically active sites in the CCL available for CO_2 conversion reactions. Furthermore, the BPM cell also exhibits a high FA oxidation rate in the ACL, which further decreases the overall cell efficiency for formic acid generation.

Fig. 7 shows the pH variation in the cathode and membrane domains for the three cell architectures. The AEM-OER cell, Fig. 7a, exhibits a constant pH of about 10.5 across all simulated current densities in the CCL domain. With increasing current density, the pH in the AEM decreases, reaching a minimum of about 9.6 at 0.5 A cm^{-2}. Fig. 7b demonstrates that the cell current significantly affects pH in the AEM-HOR cell. Near open circuit, the pH is relatively constant at around 9.5 and monotonically increases with increasing current, reaching a maximum of about 12.5 in the CCL at 0.5 A cm^{-2}. Fig. 7c shows that the pH is relatively unaffected by current density in the BPM cell, with the profile dominated by the drop from $\sim$11 to 0 at the AEL|CEL interface. Across the three architectures, the average pH in the CCL domain is observed to be: AEM-OER $<$ AEM-HOR cell $<$ BPM cell.[5,70,71]

Fig. 8 shows total transference numbers in the CCL for the AEM-OER and AEM-HOR cells at 0.5 A cm^{-2}. The transference number in either IM or LE is defined as a ratio of the ionic current from a species in the IM or LE phase to total ionic current from all species in the CCL domain (combined IM and LE current). Fig. 8a shows the transference numbers for species in both IM and LE phases of CCL in the AEM-OER cell. The ionic current in the LE phase of the cell reaches up to 75% at the AEM|CCL boundary, highlighting the importance of the

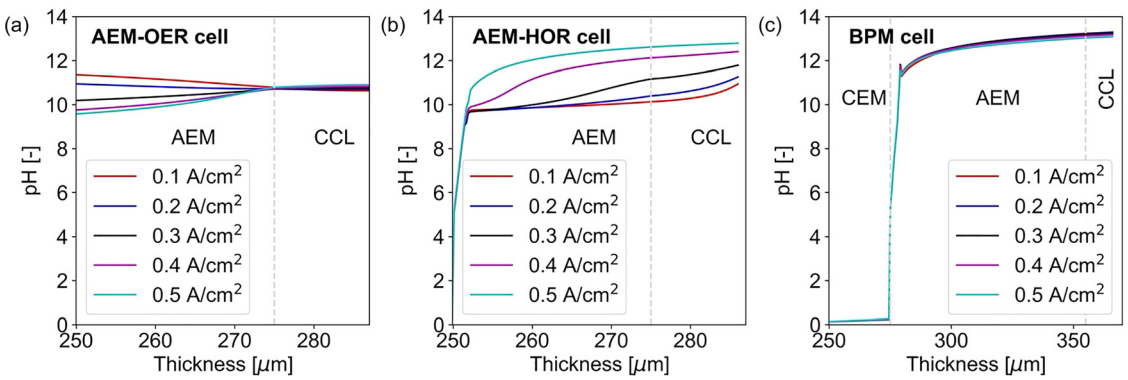

Fig. 7 pH variation in AEM-OER (a), AEM-HOR (b) and BPM cell (c) as a function of current density.

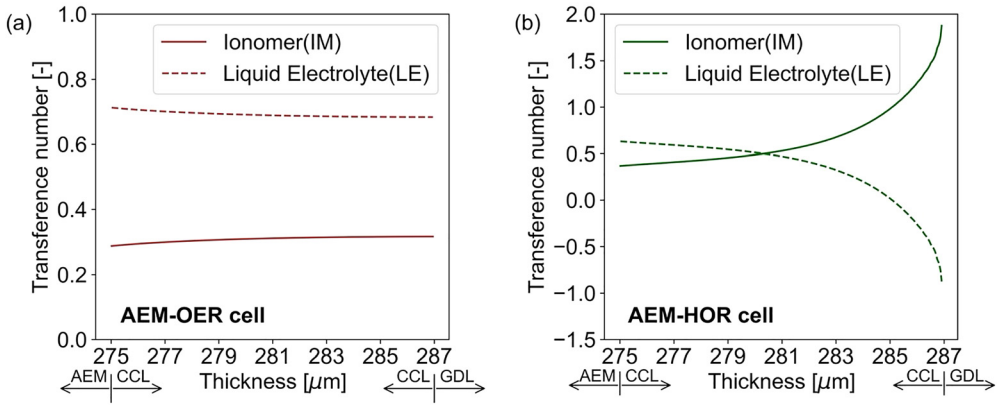

Fig. 8 Transference number for the AEM-OER cell (a) and AEM-HOR cell (b) in IM and LE domains operated at 0.5 A cm^{-2}.

liquid supporting electrolyte. Importantly, the current contributions from both LE and IM phases are almost stable along the CCL thickness. The AEM-HOR cell (Fig. 8b) features slightly more balanced ion transport in both the phases from the AEM|CCL interface until mid-way of the CCL thickness (about 280 μm). Beyond this point, the ionic current in LE and IM phases is more dynamic attributed to liquid electrolyte introduction at the CCL|GDL interface. The individual species transport is more complex in the CCL region for the AEM-HOR cell. For example, as shown in Fig. S12, K^+ and OH^- have equal and opposite transference numbers due to the KOH feed at the cathode side of the AEM-HOR cell. This causes the individual profiles for each phase to be nonlinear, especially near the CCL|GDL end. The ionic current in the IM phase of the AEM-HOR cell is slightly higher than that of the AEM-OER cell, due to the liquid electrolyte feed direction which enhances the ion transport especially for OH^- in the IM phase. The transference numbers for individual species in the entire MEA are shown in more detail in Section S12.

3.3. CO_2 utilization comparison

Fig. 9 depicts the CO_2 utilization in the cathode region for the cell architectures studied here. The CO_2 utilization is defined as the ratio of carbon dioxide consumed for electrochemical products to total CO_2 consumed in the cathode region. Detailed definitions for these calculations are given in Section S12. The considered CO_2 utilization categories are (i) electrochemical CO_2 conversion, (ii) (bi)carbonate generation, and (iii) absorption from the gas phase to aqueous CO_2. Near open circuit, all cells feature mostly (bi)carbonate generation, as this is the natural consequence of CO_2 absorption in the absence of an applied voltage. In the AEM-OER cell (Fig. 9a), electrochemical CO_2 utilization is about 38% at low current densities and increases to 62% at 0.5 A cm^{-2}. This is due to the high FE to $HCOO^-$ at high current densities, which reduces the availability of CO_2 for (bi)carbonate formation and crossover. About 2% of the supplied CO_2 is absorbed into the cell but remains unreacted.

Fig. 9b shows analogous results for the AEM-HOR cell. At low currents, this cell features ~15% electrochemical CO_2 utilization which increases to a maximum of about 25% at 0.3 A cm^{-2}. Above 0.3 A cm^{-2} in the cell the electrochemical utilization drops off due to the change in selectivity from CO_2 conversion to the HER (as demonstrated in Fig. 9c). As a result, this cell features much higher (bi)carbonate crossover (70–80%) compared to the AEM-OER cell. Similar CO_2 utilization trends are seen in the BPM cell, shown in Fig. 9c. Like the AEM-HOR cell, the BPM cell also features high (bi)carbonate crossover combined with even lower electrochemical CO_2 utilization (about 5 to 8% across the current density range). About 10% of the supplied CO_2 remains unreacted in the system as aqueous CO_2.

The AEM-HOR and BPM cells both feature KOH supplied to the cathode side. While the higher pH (see Fig. 7) creates a

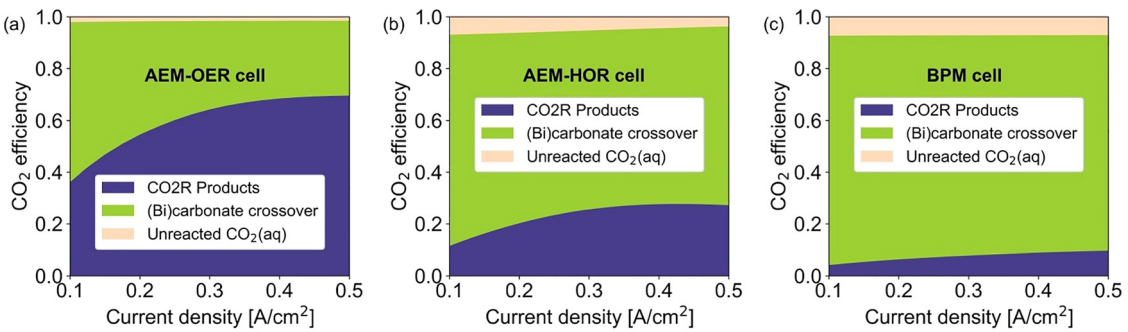

Fig. 9 CO_2 utilization inside the cathode region for the (a) AEM-OER cell (b), AEM-HOR cell (c) and BPM cell.

favorable environment for electrochemical CO_2 conversion, it also results in more carbonate formation. The acidic anode environments of these cells also support the creation of formic acid (one of the targeted goals for MEA cells). This tradeoff must be quantified, *e.g.*, *via* techno-economic analysis, to determine the relative value of the formic acid product compared to the additional wasted CO_2. This further highlights the importance of developing CCLs with good ionic conductivity which can eliminate the need for the supporting KOH electrolyte and improve electrochemical CO_2 utilization even with lower pH cathode environments. Overall, based on CO_2 utilization analysis, cells with KOH fed to the anode side tend to have better selectivities to CO_2 reduction resulting in better single pass conversion efficiency.

3.4. Voltage breakdown analysis

Voltage breakdown analyses (VBA) for the AEM-OER and AEM-HOR cells are shown in Fig. 10. VBA is a powerful technique for assessing cell performance by quantifying various individual sources of overpotentials in a system. In CO_2 electrolyzer systems, VBAs are especially valuable due to the presence of multiple electrochemical reactions and complex species transport. In Fig. 10, overpotentials are classified as thermodynamic, kinetic, and ohmic. The total ohmic loss corresponds to both electrical contact resistance and the ionic resistance of the MEA. The kinetic losses at the cathode come from the HER (acidic and basic), and CO_2 conversion into CO (CO_2CO) and formate (CO_2For). Kinetic losses at the anode come from formic acid oxidation (FAO), the HOR (for the AEM-HOR and BPM cells), and the OER (for AEM-OER cell). In the CCL, electrochemical reactions are separately accounted for at the catalyst|IM and catalyst|LE interfaces. The ohmic overpotential terms are comprised of both ionic and electronic transport losses and are lumped into a single term for simplification (since all cells are expected to have the same electronic losses). Expressions for calculating the individual overpotentials are shown in the Section S12.[63,72]

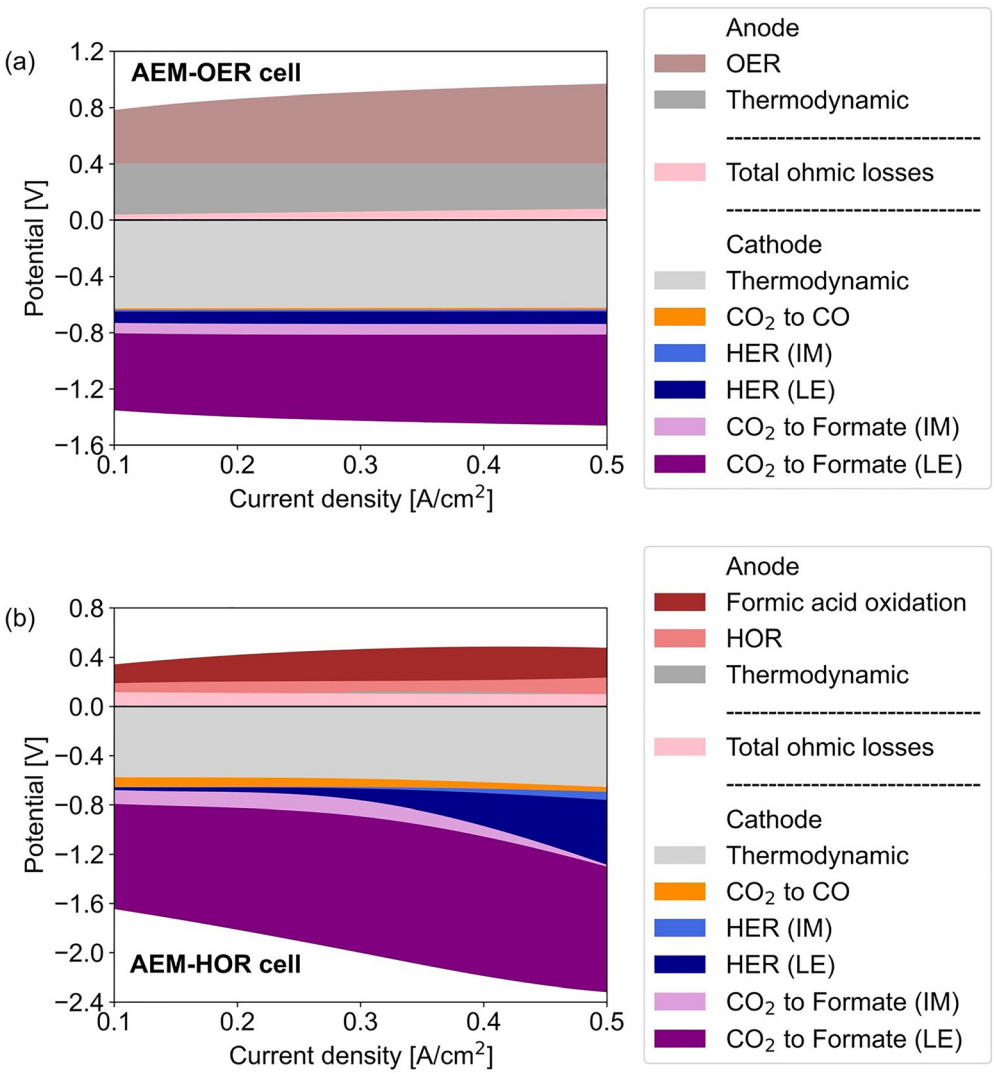

Fig. 10 Voltage breakdown analyses for the (a) AEM-OER cell (b) and AEM-HOR cell operated with 10% ionomer coverage over the cathode catalyst and 60 °C.

Fig. 10a shows the VBA for the AEM-OER cell as a function of current density. A major portion of the voltage is utilized to overcome the thermodynamic barrier in both the cathode and anode and corresponds to almost 40–50% of the total voltage (depending on the operating current). The next largest overpotential comes from the kinetics of the CO_2For reaction. Notably, almost all of the CO_2For occurs at the catalyst|LE interface as opposed to catalyst|IM. The OER activation losses are slightly lower than the CO_2For, amounting to about 550 mV at 0.5 A cm^{-2}, in good agreement with the AEM literature.[40] The remaining overpotentials in the AEM-OER cell stem from HER activation, CO_2CO activation, and ohmic losses, which are minimal in comparison.

Fig. 10b shows the VBA for the AEM-HOR cell operated between 0.1 and 0.5 A cm^{-2}. The thermodynamic potential for the acidic HOR at the anode is negligible, which reduces the open circuit potential to 0.62 V compared to 1.02 V for the AEM-OER cell. Roughly 5% of the total voltage is used for overcoming ohmic losses in the cell, which are almost constant over the current density range. Kinetic overpotentials from the anode consist of 0.11 V from the HOR and 0.15–0.26 V from FAO at 0.5 A cm^{-2}. In the AEM-HOR cell, cathode kinetic overpotentials add up to 55% of the cell voltage, which is about 15% more than the cathode kinetic losses in the AEM-OER cell. The HER overpotential regions start increasing around 0.3 A cm^{-2} as the selectivity switches from CO_2For to the HER due to the lack of CO_2 availability. The VBAs highlight CO_2 availability as a significant driver of both faradaic efficiency and cell voltage. This VBA is an important aspect to foresee the pathways for the cell improvement. The VBA plot for the BPM cell is shown in Fig. S14.

3.5. Ionomer coverage and electrolyte flow conditions

A sensitivity analysis of the cathode ionomer coverage was performed for the AEM-OER and AEM-HOR cells to elucidate its influence on the cell performance. The ionomer coverage (based on the catalyst surface area) was varied from 5% to 80%, to study the variation in cell voltage and formate partial current density (i_{HCOO^-}) from the IM and LE phases. The 10% ionomer coverage is the baseline value used for simulations in the preceding sections. The polarization curves as a function of ionomer coverage for the AEM-OER cell are shown in Fig. 11a. A minimal deviation in the voltage trends is observed for the wide range of coverage values implying that ionomer coverage has almost no impact on the cell voltage. We attribute this to the LE phase enabling the electrochemical reactions at catalyst|pore interfaces and compensating for ionic current loss. A similar pattern was observed for the AEM-HOR cell and is not shown here.

Fig. 11b shows the partial current density for formate generation, including both ionomer and liquid electrolyte domains as a function of ionomer coverage for the AEM-OER and AEM-HOR cells operated at 0.5 A cm^{-2}. In both cells, as ionomer coverage increased, the formate partial current from the IM phase increased, while the contribution from the LE phase decreased. For the AEM-OER cell, the overall partial current density (combined contribution from IM and LE phases) remained almost constant over the range of ionomer coverage and exhibited a linear relationship for i_{HCOO^-} as a function of ionomer coverage. At lower ionomer coverage (20%), about 80% of ionic current was contributed by the LE phase, while at higher ionomer coverage (80%), almost 85% of the ionic current originated from the IM phase. In other words, the relation between ionomer coverage and the formate current from each phase is roughly linear for the AEM-OER cell. In contrast, for the AEM-HOR cell, the trend for both phases was nonlinear and the overall formate partial current decreased as ionomer coverage increased. This behavior arises from the lack of CO_2 availability in the cathode at this operating current density, which negatively impacts formate generation at higher ionomer coverage levels. Moreover, the LE phase contributed approximately 65% of the current at 20% ionomer coverage, while the IM phase contributes around 50% of the current at 80% coverage. A variation exceeding 15% was noted in the AEM-HOR cell, compared to only 5% deviation in the AEM-OER cell.

A sensitivity study of the LE molarity and flow rate as a function of ionomer coverage was also conducted to better understand the role of LE in these cells. The molarity was varied between 0.2 and 1 M and the flow rate was varied to 40, 60, and 80 ml min^{-1} for the AEM-OER cell. As shown in Fig. 11c and d, variations in molarity and flow rates for the electrolyte had an insignificant effect on the formate partial current and cathode potential for the AEM-OER cell. Since the LE is fed from the anode side in this architecture, variations in LE flow conditions have a minimal impact on CCL electrochemical operation. With the aim of determining an optimal LE flow rate, a range of values were numerically tested beyond those mentioned in Fig. 11d. The cell became non-operational at flow rates lower than 30 ml min^{-1} for 10% coverage and was able to achieve a minimum operational flow rate of 22 ml min^{-1} only when the CCL featured perfect ionomer coverage (100%). Therefore, the AEM-OER cell exhibits optimal performance with flow rates above 30 ml min^{-1}, but a flow rate below the critical value (22 ml min^{-1} in this case) results in a depletion of hydroxide ions in the anode region, leading to cell failure. Additionally, changes in electrolyte molarity had no effect on formate generation for catalyst layers with more than 40% ionomer coverage, regardless of the operating current density. Further analysis of these results is provided in Section S13.

The molarity was varied similarly for the AEM-HOR cell, but the flow rate was altered to 1, 2 and 4 ml min^{-1}. Unlike the AEM-OER cell, the AEM-HOR cell displayed significant deviations with changes to molarity and flow rates. Regarding the molarity sensitivity shown in Fig. 11e, there was little variation for molarity values between 0.2 and 0.8 M, and the formate partial current from the IM phase increased linearly as ionomer coverage increased. However, the formate partial current drastically decreased at 1 M, depicting a similar pattern to the one shown in Fig. 11b. This is attributed to the formation of (bi)carbonate from OH^- ions, which reduces the availability of CO_2 for $HCOO^-$ generation. As shown in Fig. 11f, the formate

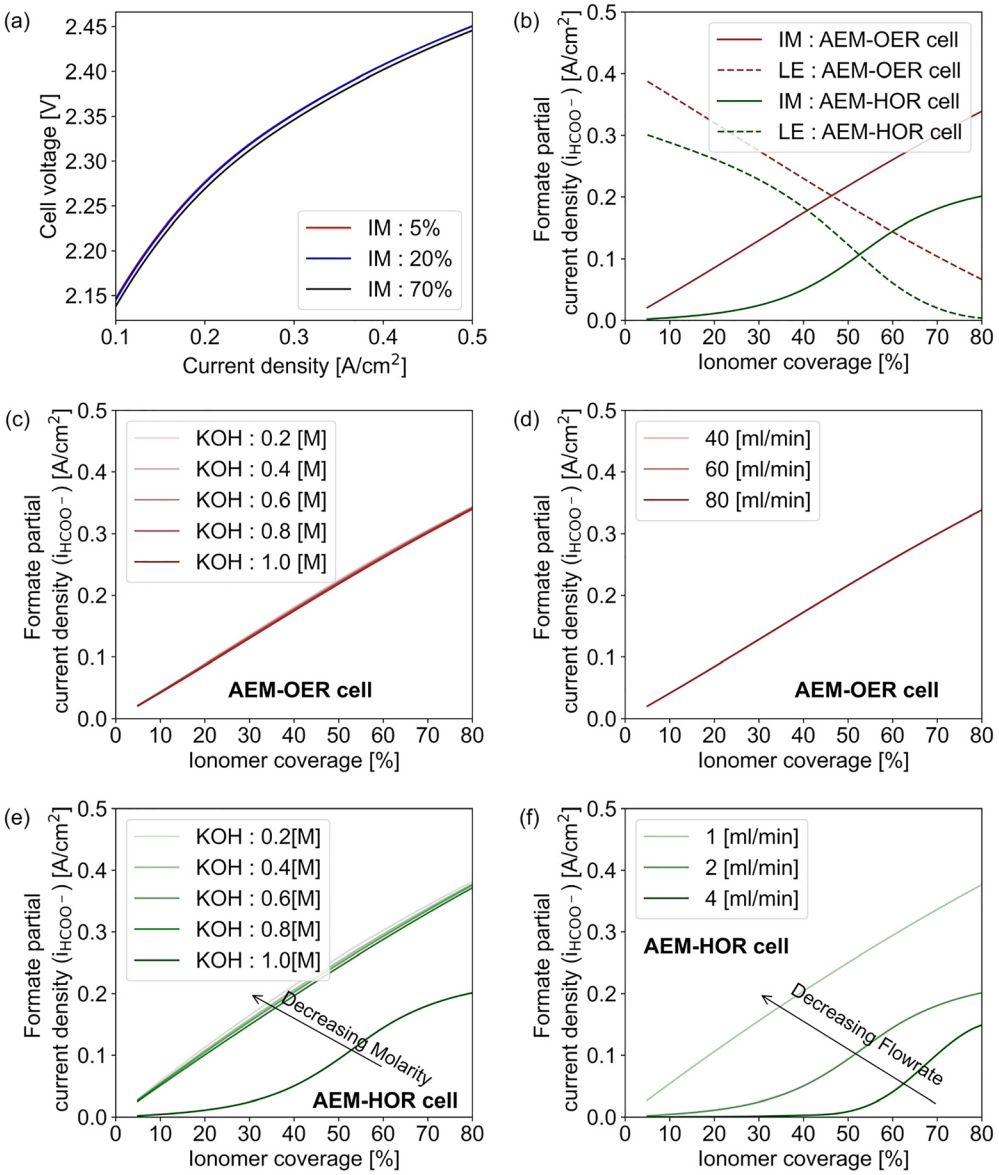

Fig. 11 Sensitivity analysis of cell performance as a function of ionomer coverage with respect to the polarization curve (a), formate partial current density as a function of ionomer coverage (b), formate partial current density from the ionomer as a function of electrolyte molarity with a 60 ml min^{-1} feed rate (c), and the anode electrolyte flow rate at electrolyte molarity of 1 M (d) for the AEM-OER cell, formate partial current density from the ionomer as a function of electrolyte molarity with a 2 ml min^{-1} electrolyte feed rate (e) and flow rate at electrolyte molarity of 1 M (f) for the AEM-HOR cell.

partial current decreases as the KOH flow rate increases. There are two main drivers of this trend: (i) increased supply of KOH to the CCL hinders the CO_2 to formate reaction due to a Le Chatelier-like equilibrium shift in eqn (9), and (ii) increased OH^- drastically increases (bi)carbonate generation, limiting the available CO_2.

From the above analyses, we conclude that the role of LE is not critically important if it is fed from the anode side. However, for MEA architectures where the electrolyte is fed to the cathode end, the LE flow rate has a significant impact on electrochemical performance since it alters the pH range in the cathode domain. Sensitivity analyses for various factors such as diffusivity, kinetics, and geometrical parameters of the cell are detailed in Section S14. These studies outline how MEA cells might be engineered to become nearly LE-free in the future.

4. Conclusion

A continuum model coupled with experimental data was employed to study the complex transport phenomena in MEA cell architectures for synthesizing formate/formic acid from CO_2. The model employed a system of generalized modified Poisson–Nernst–Planck equations to accurately consider the mixed ionic species transport, including steric effects in concentrated electrolyte environments. Electrochemical reactions

were considered at both catalyst/ionomer and catalyst/liquid electrolyte interfaces in the cathode domain. Additionally, special attention was paid to the distribution of current density at the intersection of the membrane, ionomer, and liquid electrolyte. This advanced modeling approach aids in elucidating the ionic transport mechanism in the ionomer and liquid electrolyte phase around the catalyst in the cathode. We studied three MEA cell configurations to investigate the impact of the cell architecture on cell voltage, faradaic efficiency, and reactant and product distribution. Model predictions for all three configurations were validated to experimental data for the polarization curve and cathode partial current densities.

Our analysis showed that an AEM cell performing oxygen evolution at the anode exhibited 80% faradaic efficiency to formate generation, which was the highest of the three configurations studied. We also studied an AEM cell performing hydrogen oxidation at the anode. While this configuration led to lower cell voltages, it also exhibited lower formate faradaic efficiency with significant hydrogen evolution at higher current densities. This phenomenon was traced to decreased CO_2 availability due to preferential (bi)carbonate formation in the cathode. Lastly, no meaningful conclusions about the performance of the BPM cell were possible, as it catastrophically failed due to CO_2 gas buildup at the AEL|CEL interface where (bi)carbonates recombined with H^+ from the anode (a phenomenon which was captured by the model). We include this result to highlight the importance of gas and product removal strategies, and to position our modeling approach to be capable of studying such systems in the future.

We also investigated the role of a supporting electrolyte (KOH) and found that while the K^+ ions can improve both conductivity and electrochemically active surface area in the cathode, the presence of OH^- ions raises the pH and leads to deleterious formation of (bi)carbonates. This is why the AEM-OER cell (which introduced KOH to the anode side) featured less (bi)carbonate formation and greater FE to formate than the AEM-HOR cell (which introduced KOH to the cathode side). For this reason, the ionomer coverage in the cathode is believed to be a critical factor affecting cell performance; with sufficient ionic conductivity and catalyst accessibility, the need for a supporting electrolyte could be eliminated. To this end, we also performed a parametric study on the concentration and flow rate of supplied KOH to the cell, which revealed that high ionomer coverage enabled the use of lower KOH concentrations and flow rates.

In the homogenized 1D representation, advanced electrode features like partial flooding, wetting behavior, and transport bottlenecks were not captured. In future work, we intend to focus on these aspects in more detail using 2D and 3D models to more accurately predict viable electrode designs and operating strategies to maximize CO_2 utilization and conversion.

Conflicts of interest

There are no conflicts of interest to declare.

Data availability

All data for this article were generated using the governing equations described in the main text and supplementary information (SI) using COMSOL Multiphysics® v6.4. Supplementary information contains additional modeling and experimental details, supporting results, and additional discussion. See DOI: **https://doi.org/10.1039/d5ey00272a**.

Acknowledgements

This work was authored by the National Renewable Energy Laboratory for the U.S. Department of Energy (DOE) under Contract No. DE-AC36-08GO28308. This work was funded by U.S. Department of Energy Bio Energy Technology Office. The authors acknowledge the support of Holly Gadpaille, Cole Delery, Jacob McCloud and Ellis Klein related to the maintenance and capability improvements for the analytical and testing equipment utilized in this study.

Disclaimer

The views expressed in the article do not necessarily represent the views of the DOE or the U.S. Government. The publisher, by accepting the article for publication, acknowledges that the U.S. Government retains a nonexclusive, paid-up, irrevocable, and worldwide license to publish or reproduce the published form of this work, or allow others to do so, for U.S. Government purposes.

References

1 S. Kaneco, H. Katsumata, T. Suzuki and K. Ohta, *Energy Fuels*, 2006, **20**, 409–414.
2 R. L. Cook, R. C. MacDuff and A. F. Sammells, *J. Electrochem. Soc.*, 1990, **137**, 607.
3 Y. C. Li, D. Zhou, Z. Yan, R. H. Gonçalves, D. A. Salvatore, C. P. Berlinguette and T. E. Mallouk, *ACS Energy Lett.*, 2016, **1**, 1149–1153.
4 Y. Chen, A. Vise, W. E. Klein, F. C. Cetinbas, D. J. Myers, W. A. Smith, T. G. Deutsch and K. C. Neyerlin, *ACS Energy Lett.*, 2020, **5**, 1825–1833.
5 L. Hu, J. A. Wrubel, C. M. Baez-Cotto, F. Intia, J. H. Park, A. J. Kropf, N. Kariuki, Z. Huang, A. Farghaly, L. Amichi, P. Saha, L. Tao, D. A. Cullen, D. J. Myers, M. S. Ferrandon and K. C. Neyerlin, *Nat. Commun.*, 2023, **14**, 7605.
6 X. Lu, D. Y. C. Leung, H. Wang, M. K. H. Leung and J. Xuan, *ChemElectroChem*, 2014, **1**, 836–849.
7 S. Kaneco, R. Iwao, K. Iiba, K. Ohta and T. Mizuno, *Energy*, 1998, **23**, 1107–1112.
8 K. S. Udupa, G. S. Subramanian and H. V. K. Udupa, *Electrochim. Acta*, 1971, **16**, 1593–1598.
9 J. E. Huang, F. Li, A. Ozden, A. Sedighian Rasouli, F. P. García de Arquer, S. Liu, S. Zhang, M. Luo, X. Wang, Y. Lum, Y. Xu, K. Bertens, R. K. Miao, C.-T. Dinh, D. Sinton and E. H. Sargent, *Science*, 2021, **372**, 1074–1078.
10 J. Wang, Y. Zhang, H. Bai, H. Deng, B. Pan, Y. Li and Y. Wang, *Angew. Chem.*, 2024, **63**, 1–7.

11 K. Xie, R. K. Miao, A. Ozden, S. Liu, Z. Chen, C.-T. Dinh, J. E. Huang, Q. Xu, C. M. Gabardo, G. Lee, J. P. Edwards, C. P. O'Brien, S. W. Boettcher, D. Sinton and E. H. Sargent, *Nat. Commun.*, 2022, **13**, 3609.
12 S. Moret, P. J. Dyson and G. Laurenczy, *Nat. Commun.*, 2014, **5**, 4017.
13 W.-H. Wang, Y. Himeda, J. T. Muckerman, G. F. Manbeck and E. Fujita, *Chem. Rev.*, 2015, **115**, 12936–12973.
14 A. Álvarez, A. Bansode, A. Urakawa, A. V. Bavykina, T. A. Wezendonk, M. Makkee, J. Gascon and F. Kapteijn, *Chem. Rev.*, 2017, **117**, 9804–9838.
15 J. Eppinger and K.-W. Huang, *ACS Energy Lett.*, 2017, **2**, 188–195.
16 C. Rice, S. Ha, R. I. Masel, P. Waszczuk, A. Wieckowski and T. Barnard, *J. Power Sources*, 2002, **111**, 83–89.
17 B. Loges, A. Boddien, H. Junge and M. Beller, *Angew. Chem., Int. Ed.*, 2008, **47**, 3962–3965.
18 A. Boddien, D. Mellmann, F. Gärtner, R. Jackstell, H. Junge, P. J. Dyson, G. Laurenczy, R. Ludwig and M. Beller, *Science*, 2011, **333**, 1733–1736.
19 T. Windman, N. Zolotova, F. Schwandner and E. L. Shock, *Astrobiology*, 2007, **7**, 873–890.
20 H.-H. Wang, S.-N. Zhang, T.-J. Zhao, Y.-X. Liu, X. Liu, J. Su, X.-H. Li and J.-S. Chen, *Sci. Bull.*, 2020, **65**, 651–657.
21 N. Pearcy, M. Garavaglia, T. Millat, J. P. Gilbert, Y. Song, H. Hartman, C. Woods, C. Tomi-Andrino, R. R. Bommareddy, B.-K. Cho, D. A. Fell, M. Poolman, J. R. King, K. Winzer, J. Twycross and N. P. Minton, *PLoS Comput. Biol.*, 2022, **18**, e1010106.
22 C. Johnson, *Annu. Merit Rev.*, 2023, 1–32.
23 B. S. Crandall, T. Brix, R. S. Weber and F. Jiao, *Energy Fuels*, 2023, **37**, 1441–1450.
24 O. Yishai, S. N. Lindner, J. Gonzalez de la Cruz, H. Tenenboim and A. Bar-Even, *Curr. Opin. Chem. Biol.*, 2016, **35**, 1–9.
25 M. Aresta, *Quím. Nova*, 1999, **22**, 269–272.
26 A. S. Agarwal, Y. Zhai, D. Hill and N. Sridhar, *ChemSusChem*, 2011, **4**, 1301–1310.
27 E. Barton Cole, P. S. Lakkaraju, D. M. Rampulla, A. J. Morris, E. Abelev and A. B. Bocarsly, *J. Am. Chem. Soc.*, 2010, **132**, 11539–11551.
28 M. Le, M. Ren, Z. Zhang, P. T. Sprunger, R. L. Kurtz and J. C. Flake, *J. Electrochem. Soc.*, 2011, **158**, E45.
29 K. Toyohara, H. Nagao, T. Mizukawa and K. Tanaka, *Inorg. Chem.*, 1995, **34**, 5399–5400.
30 L.-C. Weng, A. T. Bell and A. Z. Weber, *Phys. Chem. Chem. Phys.*, 2018, **20**, 16973–16984.
31 D. M. Weekes, D. A. Salvatore, A. Reyes, A. Huang and C. P. Berlinguette, *Acc. Chem. Res.*, 2018, **51**, 910–918.
32 B. Endrődi, A. Samu, E. Kecsenovity, T. Halmágyi, D. Sebők and C. Janáky, *Nat. Energy*, 2021, **6**, 439–448.
33 S. Zhang, P. Kang and T. J. Meyer, *J. Am. Chem. Soc.*, 2014, **136**, 1734–1737.
34 J. T. Feaster, C. Shi, E. R. Cave, T. Hatsukade, D. N. Abram, K. P. Kuhl, C. Hahn, J. K. Nørskov and T. F. Jaramillo, *ACS Catal.*, 2017, **7**, 4822–4827.
35 J. Y. Zhao, Y. Liu, W. Li, C. F. Wen, H. Q. Fu, H. Y. Yuan, P. F. Liu and H. G. Yang, *Chem. Catal.*, 2023, **3**, 100471.
36 C. P. O'Brien, R. K. Miao, S. Liu, Y. Xu, G. Lee, A. Robb, J. E. Huang, K. Xie, K. Bertens, C. M. Gabardo, J. P. Edwards, C.-T. Dinh, E. H. Sargent and D. Sinton, *ACS Energy Lett.*, 2021, **6**, 2952–2959.
37 Y. Xu, J. P. Edwards, S. Liu, R. K. Miao, J. E. Huang, C. M. Gabardo, C. P. O'Brien, J. Li, E. H. Sargent and D. Sinton, *ACS Energy Lett.*, 2021, **6**, 809–815.
38 L. Pilon, H. Wang and A. d'Entremont, *J. Electrochem. Soc.*, 2015, **162**, A5158.
39 K. R. Disselkoen, J. A. Rabinowitz, A. Mani and M. W. Kanan, *ACS Sustainable Chem. Eng.*, 2024, **12**(19), 7235–7245.
40 J. Liu, Z. Kang, D. Li, M. Pak, S. M. Alia, C. Fujimoto, G. Bender, Y. S. Kim and A. Z. Weber, *J. Electrochem. Soc.*, 2021, **168**, 054522.
41 J. C. Bui, C. Kim, A. J. King, O. Romiluyi, A. Kusoglu, A. Z. Weber and A. T. Bell, *Acc. Chem. Res.*, 2022, **55**, 484–494.
42 Y. Chen, J. A. Wrubel, A. E. Vise, F. Intia, S. Harshberger, E. Klein, W. A. Smith, Z. Ma, T. G. Deutsch and K. C. Neyerlin, *Chem. Catal.*, 2022, **2**, 400–421.
43 C. Chen, X. Yan, Y. Wu, S. Liu, X. Zhang, X. Sun, Q. Zhu, H. Wu and B. Han, *Angew. Chem., Int. Ed.*, 2022, **61**, e202202607.
44 V. Chanda, J. R. C. Junqueira, N. Sikdar, I. Sanjuán, M. Braun, S. Dieckhöfer, S. Seisel and C. Andronescu, *Electrochem. Sci. Adv.*, 2023, **3**, e2100200.
45 E. W. Lees, J. C. Bui, D. Song, A. Z. Weber and C. P. Berlinguette, *ACS Energy Lett.*, 2022, **7**, 834–842.
46 L.-C. Weng, A. T. Bell and A. Z. Weber, *Energy Environ. Sci.*, 2019, **12**, 1950–1968.
47 S. Verma, X. Lu, S. Ma, R. I. Masel and P. J. A. Kenis, *Phys. Chem. Chem. Phys.*, 2016, **18**, 7075–7084.
48 L. Fan, C. Xia, P. Zhu, Y. Lu and H. Wang, *Nat. Commun.*, 2020, **11**, 3633.
49 T.-D. Nguyen-Phan, L. Hu, B. H. Howard, W. Xu, E. Stavitski, D. Leshchev, A. Rothenberger, K. C. Neyerlin and D. R. Kauffman, *Sci. Rep.*, 2022, **12**, 8420.
50 K. V. Petrov, J. C. Bui, L. Baumgartner, L.-C. Weng, S. M. Dischinger, D. M. Larson, D. J. Miller, A. Z. Weber and D. A. Vermaas, *Sustainable Energy Fuels*, 2022, **6**, 5077–5088.
51 L. N. Stanislaw, M. R. Gerhardt and A. Z. Weber, *ECS Trans.*, 2019, **92**, 767–779.
52 A. Z. Weber and J. Newman, *J. Electrochem. Soc.*, 2004, **151**, A311.
53 A. Z. Weber and J. Newman, *J. Electrochem. Soc.*, 2003, **150**, A1008.
54 J. A. Wrubel, Y. Chen, Z. Ma and T. G. Deutsch, *J. Electrochem. Soc.*, 2020, **167**, 114502.
55 M. S. Kilic, M. Z. Bazant and A. Ajdari, *Phys. Rev. E: Stat., Nonlinear, Soft Matter Phys.*, 2007, **75**, 021502.
56 M. S. Kilic, M. Z. Bazant and A. Ajdari, *Phys. Rev. E: Stat., Nonlinear, Soft Matter Phys.*, 2007, **75**, 021503.
57 D. Bohra, PhD thesis, TU Delft, 2020.

58 D. Bohra, J. H. Chaudhry, T. Burdyny, E. A. Pidko and W. A. Smith, *Energy Environ. Sci.*, 2019, **12**, 3380–3389.
59 E. F. Johnson, E. Boutin, S. Liu and S. Haussener, *EES Catal.*, 2023, **1**, 704–719.
60 H. Wang, A. Thiele and L. Pilon, *J. Phys. Chem. C*, 2013, **117**, 18286–18297.
61 E. N. Butt, J. T. Padding and R. Hartkamp, *Sustainable Energy Fuels*, 2023, **7**, 144–154.
62 E. N. Butt, J. T. Padding and R. Hartkamp, *J. Electrochem. Soc.*, 2024, **171**, 014504.
63 E. W. Lees, J. C. Bui, O. Romiluyi, A. T. Bell and A. Z. Weber, *Nat. Chem. Eng.*, 2024, 1–14, DOI: **10.1038/s44286-024-00062-0**.
64 J. C. Bui, E. W. Lees, L. M. Pant, I. V. Zenyuk, A. T. Bell and A. Z. Weber, *Chem. Rev.*, 2022, **122**, 11022–11084.
65 H. Strathmann, J. J. Krol, H.-J. Rapp and G. Eigenberger, *J. Membr. Sci.*, 1997, **125**, 123–142.
66 COMSOL Multiphysics® v6.3, COMSOL AB, Stockholm, Sweden.
67 J. Hennig, M. Elfner, A. Maeder and J. Feder, *Zenodo*, 2024, DOI: **10.5281/zenodo.11539226**.
68 D. J. Higham, *SIAM J. Numer. Anal.*, 1999, **37**, 194–210.
69 P. Jayapragasam, P. L. Bideau and T. Loulou, *Numer. Heat Transfer, Part B*, 2018, **74**, 729–745.
70 M. Bahreini, M. Désilets, E. Pahija, U. Legrand, J. Guo and A. G. Fink, *Ind. Eng. Chem. Res.*, 2024, **63**, 18187–18198.
71 Q. Xu, S. Liu, F. Longhin, G. Kastlunger, I. Chorkendorff and B. Seger, *Adv. Mater.*, 2024, **36**, 1–11.
72 M. R. Gerhardt, L. M. Pant, J. C. Bui, A. R. Crothers, V. M. Ehlinger, J. C. Fornaciari, J. Liu and A. Z. Weber, *J. Electrochem. Soc.*, 2021, **168**, 074503.